Layered azimuthal anisotropy of Rayleigh wave phase velocities in the European Alpine lithosphere inferred from ambient noise

Bill Fry [a,b,*], Frédéric Deschamps [b], Edi Kissling [b], Laurent Stehly [c,d], Domenico Giardini [b]

[a] GNS Science, Wellington, New Zealand
[b] ETH-Zurich, Zurich, Switzerland
[c] Berkeley Seismological Laboratory, University of California-Berkeley, United States
[d] GEOAZUR, University of Nice, France

ARTICLE INFO

ABSTRACT

Passive seismic imaging of the earth is a rapidly developing field of study. Recent advances in noise cross correlation techniques allow imaging of isotropic surface-wave and shear-wave velocities in areas where earthquake numbers and distributions are insufficient to implement traditional earthquake based tomography. Furthermore, advances in the theory underpinning surface wave inversion have led to depth-dependent mapping of seismic anisotropy in the lithosphere and upper asthenosphere. We show that by merging these two rapidly advancing fields we can invert noise-based phase velocity measurements for azimuthally anisotropic phase speed, thereby providing a highly resolved image of layered azimuthal anisotropy in continental crust. We apply this new algorithm in the western Alps, an area of complex lithospheric structure. Alpine crustal thickening results from continental collision, indentation of the Ivrea mantle into the middle crust of the European plate, rollback of the European lithospheric mantle, and crustal slicing. We find that anisotropy beneath the central Alps is stratified in two layers — one with an orogen-parallel fast direction above ~30 km depth and another with a strong orogen-perpendicular fast direction at greater depth. Although our resolution is reduced outside the central Alps, we map orogen-parallel anisotropy in the crust of the northern Alpine foreland. We interpret the results in the central Alps as first-order evidence for a model of azimuthal anisotropy in which (1) near-vertical emplacement of crustal slices following detachment of the lithospheric mantle from the crust gives rise to orogen-parallel fast directions of wave propagation in the crust, and (2) dominantly horizontal tectonics in the thickened crustal root and uppermost mantle yield orogen-perpendicular fast directions at greater depth.

© 2010 Elsevier B.V. All rights reserved.

1. Introduction

Although the central Alps have likely been studied as long as any orogen in the world, there is still no consensus model explaining the geodynamic development of the Alpine lithosphere and uppermost asthenosphere. The Alpine orogeny resulted from the collision of the Adriatic lithosphere (promontory of the African plate) with the European plate in the Late Cretaceous (e.g. Coward and Dietrich, 1989). In the Oligocene, subducting lithosphere changed from oceanic to continental and slab breakoff likely occurred (Davies and von Blanckenburg, 1995). Much of our knowledge of the current state of the Alpine lithosphere comes from traditional body and surface wave seismic imaging which have shown high seismic velocities in the upper mantle below the Alps (Lippitsch et al., 2003; Piromallo and Morelli, 2003; Fry et al., 2008; Peter et al., 2008; Boschi et al., 2009). These high velocity anomalies have been interpreted as evidence for subducted slabs. Thickened crust in the Alps has also been imaged (Wortel and Spakman, 1993; Waldhauser et al., 1998; Lippitsch et al., 2003). Prior to our current study, tomography of the Alps has been limited to inversions for isotropic velocity structure. Seismic anisotropy information is complementary to the isotropic velocity studies and can provide constraints on geodynamic models of the region.

In response to strain, crustal (e.g., amphibole) and mantle (e.g., olivine) minerals can develop some specific fabrics that result in seismic anisotropy. The direction of fast propagation is usually the direction of maximum deformation (Christensen, 1984; Nicolas and Christensen, 1987). Seismic anisotropy beneath continents has been mapped with high-resolution using shear-wave splitting (Silver, 1996; Savage, 1999; Fouch and Rondenay, 2006), but the origin and interpretation of this anisotropy is controversial. Some measurements agree with regional tectonic structure (e.g., in collisional regimes, a direction of fast propagation that is sub-parallel to the belt), suggesting a lithospheric origin, whereas others show large scale patterns that

* Corresponding author. GNS Science, PO Box 30368, Lower Hutt 5010, New Zealand. Tel.: +64 4 579 4286; fax: +64 4 570 4600.
E-mail address: b.fry@gns.cri.nz (B. Fry).

correspond to the absolute plate motion, suggesting an asthenospheric origin. Surface waves sample different depths depending on their period. This trait provides the vertical resolution that is missing in shear-wave splitting measurements. Global and continental scale models based on surface-wave data have resolved different anisotropic patterns in the lithosphere and in the upper asthenosphere (Simons et al., 2002; Debayle et al., 2005; Marone and Romanowicz, 2007). Because of the lateral resolution of these models, relating lithospheric anisotropy to regional tectonics is difficult. However, by using data from dense arrays of seismic stations, isotropic and anisotropic anomalies can be mapped with good resolution at a regional scale (Pedersen et al., 2006; Yang and Forsyth, 2006; Zhang et al., 2007; Deschamps et al., 2008a; Eberhart-Phillips and Reyners, 2009). Layered anisotropic structure has been interpreted as resulting from both frozen and present sources, and relates to both past tectonics (Darbyshire and Lebedev, 2009) and present absolute plate motion (Deschamps et al., 2008b). Previous studies utilized earthquake sources, which are naturally spatially and temporally limited. Areas with inhomogeneous distributions of earthquakes such as the European Alps are difficult to image with these methods. Noise-based tomography does not use earthquake energy and consequently is not hindered by heterogeneous earthquake distributions. We therefore employ a method to invert ambient noise data for regional scale layered anisotropy.

2. Methods

It has been shown that the surface-wave portion of the Green's Function between two receivers can be estimated by stacking the cross correlation functions (CF) of ambient noise recorded at each of the stations (Lobkis and Weaver, 2001; Snieder, 2004; Shapiro et al., 2005; Sanchez-Sesma et al., 2006). Stacking cross correlations from each station pair statistically requires that incoherent energy propagating off the great-circle path between the stations interferes destructively; coherent energy that propagates directly between the receivers is isolated. Furthermore, taking the time derivative of the CF yields the time domain empirical Green's Function (EGF) from which reliable phase velocity estimates can be made (Sabra et al., 2005; Yao et al., 2006). However, in an ambient field resulting from a homogenous distribution of sources, extracting the phase velocities from the CF is possible if an appropriate phase correction is applied. In a homogeneous isotropic media, the phase of the CF resulting from an isotropic energy distribution is advanced from the GF by $\pi/2$ (Yao and van der Hilst, 2009). In the presence of a unidirectional energy source, the phase is still advanced, but to a lesser degree. In our study area, energy is well distributed when averaged over a year of cross correlations. In fact, at the most important periods of our study (~20 s), energy is dominated by a very wide distribution (~180°) owing to a large region of oceanic disturbances in the northern Atlantic Ocean during the northern hemisphere winter (Stehly et al., 2006). This energy distribution would therefore imply that at all inter-station azimuths, a phase correction of $\pi/2$ is appropriate to measure Rayleigh wave phase velocities. To confirm the validity of our phase correction, we have compared measurements from traditional two-station analysis to measurements made from the cross correlations along an azimuth parallel to the average trace of the central Alps.

In a directionally biased ambient wavefield, estimates of phase velocity from noise cross correlations will be azimuthally biased (Yao and van der Hilst, 2009). However, in their case study of central Asia, Yao and van der Hilst (2009) show that azimuthal bias is small and point out that spatial smoothing serves to further reduce the effects of azimuthally dependent velocity estimates on inversions for anisotropy. In the present study, we present first-order results for azimuthal anisotropy by classifying the anisotropy as either orogen-parallel or orogen-perpendicular. Small-scale variations in fast directions are not considered robust and are consequently not interpreted.

2.1. Cross correlation and phase velocity measurements

We apply a noise cross correlation and stacking procedure similar to the method of Stehly et al. (2009). Continuous data from 29 broadband (STS-2) stations in the SDSNet and 7 broadband (STS-2) stations from TomoCH have been correlated on a day-by-day basis. In this method, we first cut seismic recordings to 1-day files. The signals are then decimated to 1 Hz and the trend is removed by subtracting the best-fit line from the signal and the signals are tapered. We deconvolve the instrument responses, leaving a record of ambient velocity recorded at the site. The data are then spectrally whitened in a frequency band between 0.008 and 0.33 Hz (3 to 125 second periods). The whitening lessens the effects of spectral peaks that result from earthquakes and dominant oceanic microseismic peaks. We perform the time-domain cross correlation for the vertical component of each day of recording for each station pair. Because the particle motion of Rayleigh waves is recorded on the radial and vertical components, by looking at the vertical component, we are isolating the Rayleigh wave signal. The cross correlation functions are then stacked for each station pair. With a sufficient number of stacked correlations, the stacked-function becomes stable in our frequencies of interest. Stehly et al. (2006) found a stable CF after stacking just one year of data.

We then determine the phase information as a function of instantaneous frequency from the cross correlation function and use these data to determine the corrected phase dispersion curve with a modified 2-station method of Meier et al. (2004). Phase velocities are manually chosen to negate multiple-cycle ambiguities by comparing the obtained velocity to a background earth model and 'picking' the appropriate cycle number. Between 185 and 332 phase velocity observations were used for each inversion we present (Fig. 1).

2.2. Inversion of dispersion curves

For each inter-station path, the measured dispersion curve represents the average Rayleigh-wave phase velocity along the path as a function of period (or frequency). Following the same inversion procedure as in Deschamps et al. (2008a), we use a perturbative approach to invert our catalogue of phase velocity measurements for the isotropic and anisotropic components of phase velocity at discrete periods of observation, between 6 and 60 s, using a ray-theoretical approximation with an explicitly defined ray sensitivity width of 20 km. Deschamps et al. (2008a) noted that the inverted phase velocity model is not sensitive to the chosen ray sensitivity width. Similarly, we performed inversions for ray sensitivity widths between 10 and 100 km, but did not find significant differences in the phase velocity model.

At any given frequency, phase velocity variations in a laterally heterogeneous earth can be written as (Smith and Dahlen, 1973)

$$\delta C(\varphi, \theta) = \delta C_{iso}(\varphi, \theta) + \delta C_{2\psi}(\varphi, \theta) + \delta C_{4\psi}(\varphi, \theta) \tag{1}$$
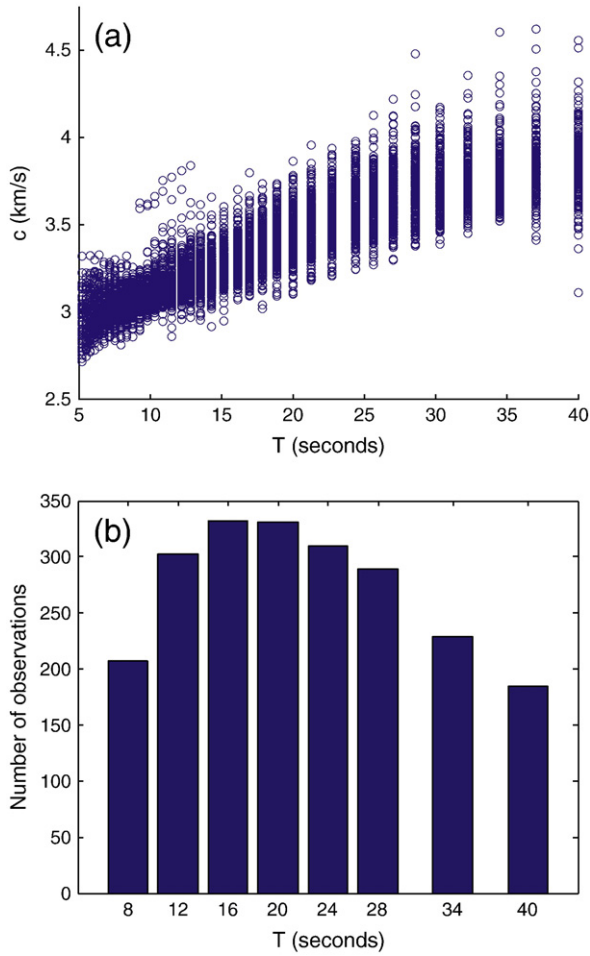
where ψ is the azimuth of anisotropy. We discretize the anisotropic contributions of wave speed as

$$\delta C_{2\psi}(\varphi, \theta) = A_{2\psi} \cos(2\psi) + B_{2\psi} \sin(2\psi) \tag{2}$$

$$\delta C_{4\psi}(\varphi, \theta) = A_{4\psi} \cos(4\psi) + B_{4\psi} \sin(4\psi).$$

The anisotropic coefficients contain information relating to both the amplitude (Λ) and direction (Θ) of the anisotropy, as defined by:

$$\begin{cases} \Lambda_{2\Psi} = \sqrt{A_{2\Psi}^2 + B_{2\Psi}^2} \\ \Theta_{2\Psi} = \frac{1}{2}\arctan\left(\frac{B_{2\Psi}}{A_{2\Psi}}\right) \end{cases} \text{ and } \begin{cases} \Lambda_{4\Psi} = \sqrt{A_{4\Psi}^2 + B_{4\Psi}^2} \\ \Theta_{4\Psi} = \frac{1}{4}\arctan\left(\frac{B_{4\Psi}}{A_{4\Psi}}\right) \end{cases} \tag{3}$$

Fig. 1. (a) Composite plot of all phase velocity dispersion curves used in this study. (b) Histogram showing the number of phase velocity observations inverted at each period.

Supplementary material, and provides a qualitative estimate of the error in our models.

Resolution tests (e.g., checkerboard tests) and resolution matrices are useful to estimate the robustness of the seismic features we observe. Fig. 3 shows resolution and tradeoff tests at $T = 20$ s, in which we prescribed test models m^{test}, calculate their associated test data following

$$d^{test} = Gm^{test}, \qquad (5)$$

and invert these test data for phase velocity maps using the procedure described above. The damping and smoothing are similar to those of our preferred model. Resolution tests (Fig. 3c–d) clearly show that the change in the anisotropy pattern between the foreland and the central chain is a robust feature. We did not perform resolution test for smaller structures. However, small features (100 km and less) may not be resolved by our model, as suggested by the smearing observed in the resolution matrices (see below, and Supplementary Fig. S1). Again, this does not alter our main interpretations and conclusions (Sections 3 and 4), since our model perfectly resolves the main

We parameterize our model space with a triangular grid consisting of 96 local cubic B-splines with an approximate spacing of 50 km, following the scheme of (Wang and Dahlen, 1995). We define the path-averaged phase velocity anomaly for each station pair (i) as

$$\overline{\delta C_i} = \int_{\varphi} \int_{\theta} K_i(\varphi, \theta) \delta C(\varphi, \theta) d\varphi d\theta, \qquad (4)$$

where K_i is the sensitivity kernel that defines the relative weight of each knot for each path (Lebedev and Van der Hilst, 2008). We then create a system of linear equations based on Eq. (4). We solve these equations for the path-averaged phase velocity anomaly for each station pair with an LSQR algorithm (Paige and Saunders, 1982) with slight norm and lateral smoothing. At each node, we calculate the 5 wave-speed parameters, including the four anisotropic coefficients ($A_{2\psi}, B_{2\psi}, A_{4\psi}, B_{4\psi}$) and the isotropic component (C_{iso}). We inverted for 4Ψ terms because their contribution was found to be non negligible (Montagner and Tanimoto, 1991; Trampert and Woodhouse, 2003). As previously shown in another regional study (Deschamps et al., 2008a,b), we observe that the 4Ψ terms are comparable to the 2Ψ terms in amplitude, but that their contribution is not needed to explain the data, i.e. the improvement in the data fit due to the 4Ψ terms is statistically not significant. Therefore, in the remainder of this paper, we will focus our interpretation on the 2Ψ terms only.
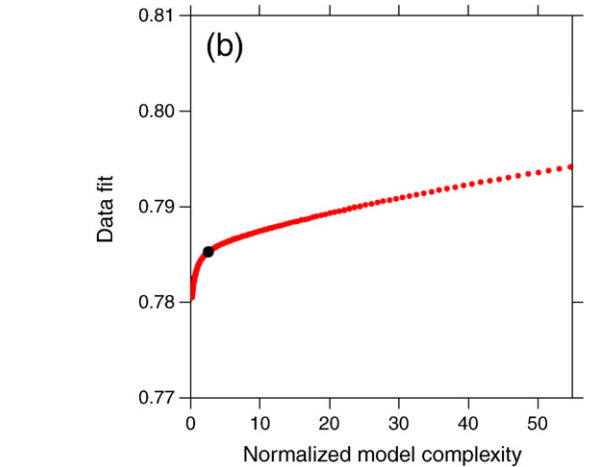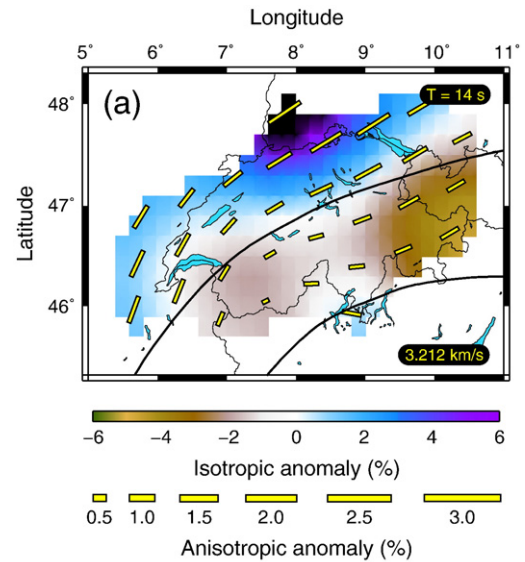
We use a standard L-curve analysis to determine an acceptable suite of models and then choose our final model from that suite (e.g. Fig. 2). An animation showing the tradeoff between model complexity, damping, and data fit for the inversion at 14 s is shown in the online

Fig. 2. (a) Isotropic and 2Ψ anisotropy anomalies from our preferred model at 14 s. Yellow bars are oriented in the direction of fast wave propagation and scaled to the percent deviation from the average isotropic value. (b) Plot of model complexity versus data fit. The black dot represents the point on the curve where our preferred model resides.
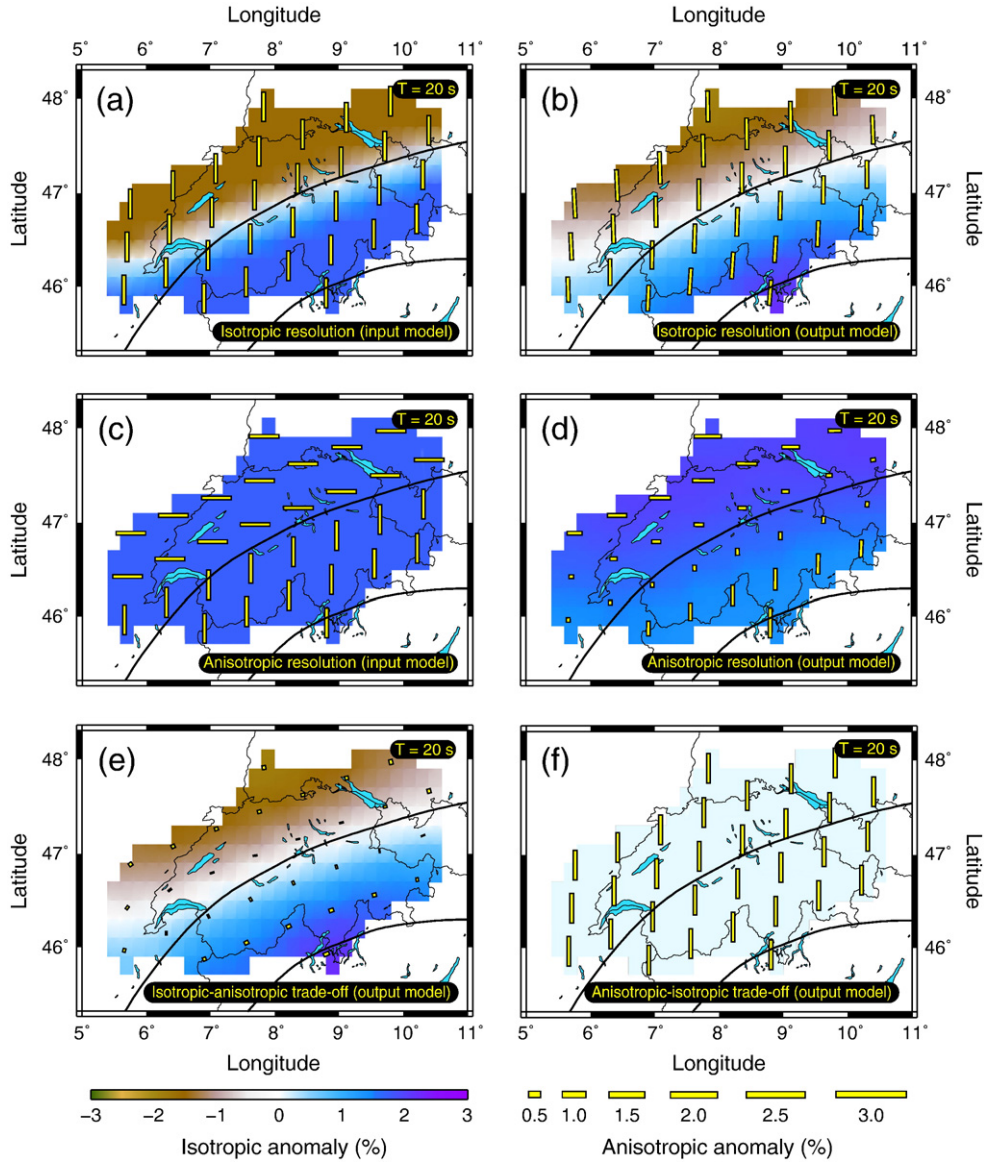
Fig. 3. Resolution test and tradeoffs between isotropic and anisotropic anomalies at 20 s period. (a) Input and (b) output models of the resolution test for isotropic terms. (a) Input and (b) output models of the resolution test for isotropic terms. (c) Input and (d) output models of the resolution test for anisotropic terms. (e–f) Tradeoffs between isotropic and anisotropic anomalies. The input model for plot (e) is like in plot (a), but with anisotropy switched to zero. The input model for plot (f) is like in plot (a), but with isotropic anomalies switched to zero.

structure in this region (i.e., the dichotomy between the Alpine foreland and the central chain).

Resolution matrices are less intuitive (they are not presented in the form of maps), but they provide valuable information about the amount of tradeoffs between the inverted parameters, in particular between the isotropic and anisotropic terms.

The least squares solution to the inverse problem is

$$x_{LS} = (A^T A + D)^{-1} A^T d, \qquad (6)$$

where A is a matrix related to the sensitivity kernels and model parameterization, D is a damping matrix containing the sum of our norm and roughness regularization, and d is the vector containing phase velocity variance from a starting model. We can then define a resolution matrix R as (Trampert and Lévêque, 1990)

$$R = (A^T A + D)^{-1} A^T A. \qquad (7)$$

This matrix directly quantifies the relative contribution of neighbouring parameters in the solution of the inverse problem at adjacent nodes of our model. With ideal resolution, $R = I$, where I is the identity matrix. However, with real data, the off-diagonal elements of the resolution matrix will not equal zero. Each of these off-diagonal elements represents the relative contribution of neighbouring free parameters to the solution at each node. We plot the resolution matrix for the 20 s period inversion in Fig. S1. While there is lateral smearing in the inversion, the lack of energy on the off-diagonals and show there is little tradeoff in the mapping of isotropic and anisotropic parameters, as also indicated by the sensitivity tradeoff test at 20 s period (Fig. 3e–f).

3. Results

We present our preferred models of 2ψazimuthal anisotropy at 8, 12, 16, 20, 24, 28, 34, and 40 second periods in Fig. 4. It should be noted that this is the horizontal component of the 3D anisotropy. As such, it is a
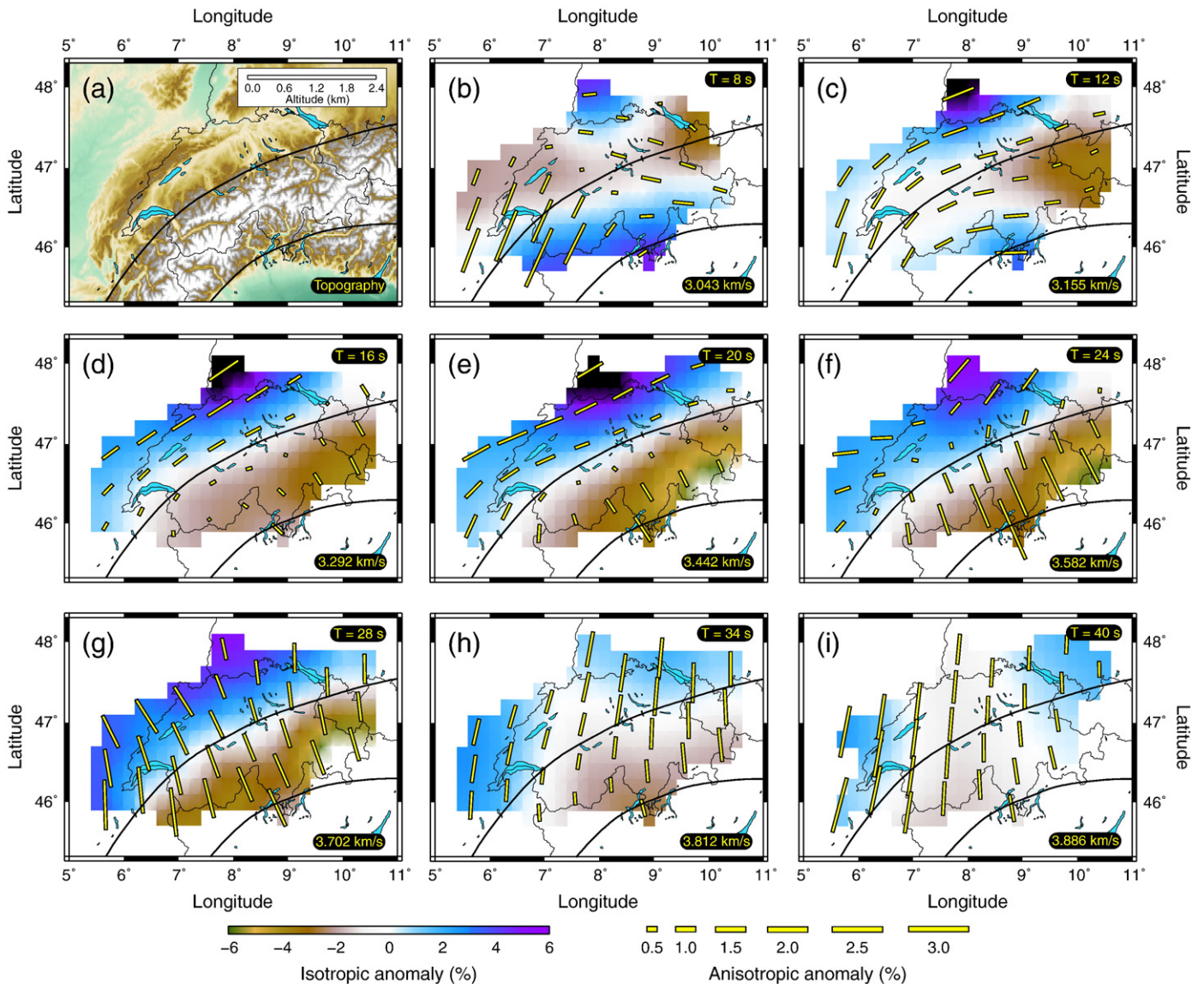
Fig. 4. The first panel shows topography of the central Alps overlain with the 2 black curves representing the Alpine front to the north and Adriatic front to the south. The remaining panels show our preferred models of isotropic (color scale) and anisotropic (yellow bars) Rayleigh-wave velocity anomalies at 8, 12, 16, 20, 24, 28, 34, and 40 second periods. Isotropic anomalies are relative to the regional average isotropic velocity (value on each panel). As in Fig. 2, yellow bars show direction of the fast 2Ψ axis and are scaled to percent deviation from the regional average isotropic velocity. Background colors indicate isotropic.

minimum possible value of the total anisotropy. The dominant fabric in the models for 8 s, 12 s, and 16 s, sampling the upper 20 to 30 km of the crust, as indicated by depth sensitivity kernels (Fig. 5), is an orogen parallel fast direction with roughly 1 to 2 % faster speeds. In contrast, at periods equal to and greater than 24 s (sampling depths between 30 and 70 km), we observe an orogen perpendicular fast direction. The amplitude of anisotropy is comparable, but slightly larger (1.5–2.5 %) than that observed in the 8–16 s range. Models at intermediate periods (20 s and around) show intermediate patterns in between those observed in the 8–16 s and 24–28 s ranges. We retrieve stable models up to ~60 s period. In these models, we image roughly orogen perpendicular fabric with anisotropy amplitudes of ~1–2%. It should be noted however, that with increasing period and a subsequent increase in the wavelength/path-length ratio and decreasing number of data, the data have reduced ability to resolve fine-scale lateral heterogeneities. The patterns observed in the ranges of 8–16 s and 24–28 s are robust and stable with a wide range of imposed regularization as can be seen in an L-curve animation in online

Supplementary material. This shows the fast direction remains stable, even with relatively small values of the smoothing coefficient. Fig. 5 indicates that sensitivity kernels for periods equal to or smaller than 16 s (those with orogen-parallel anisotropy) barely overlap those for periods equal to or larger than 24 s (those with orogen-perpendicular anisotropy), suggesting that the anisotropy we observe beneath the central Alps is stratified in two layers, with a boundary approximately located around 30 km-depth. Anisotropy in each layer may have different geodynamic origins. In the northern foreland of the Alps, anisotropy is also layered. However, the orogen-parallel fabric is pervasive throughout the crust and possibly results from 'frozen' anisotropy created during one of the documented pre-alpine orogenic events. However, resolution of our inversions outside the central Alps is limited and our current data are incapable of resolving fine-scale lateral variations in this area. The patterns we observe at 34–40 s are also well resolved (they rely on at least 150 observations, Fig. 1b) and stable regarding the regularization, but they sample a thicker layer, e.g. from about 40 km to 120 km for T = 40 s (Fig. 5). The patterns we observe at
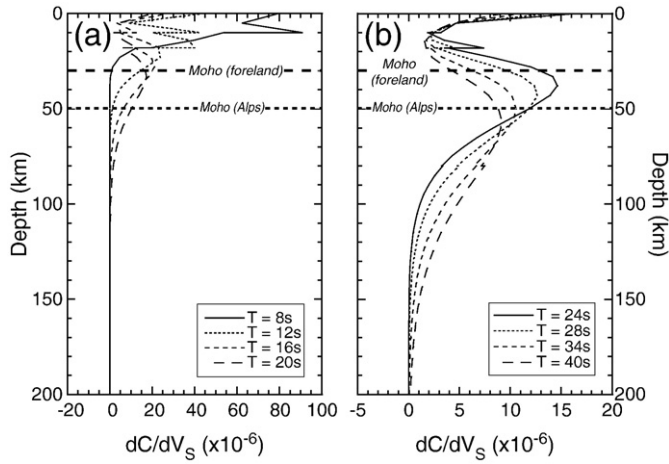
Fig. 5. Partial derivatives calculated from input 1D model for each of the periods shown in Fig. 4 for periods between (a) 8 and 20 s, and (b) 24 and 40 s. The curves show the depth-dependence of the fundamental modes at each period. Note that the x-axis scales in plots (a) and (b) are different. For comparison, the horizontal thick dashed lines represent the Moho depth beneath the foreland and beneath the Alps.

34–40 s periods are mostly imaging fabrics located in the lithospheric mantle, and therefore related to the slab motion, but they may also be biased by fabrics located in the lower crust, which, as indicated by our inversion, have a different direction.

4. Discussion and conclusion

Inversion of our dispersion curves for an anisotropic regional model of Rayleigh wave phase velocity in the central Alps strongly suggest that azimuthal anisotropy beneath this region is vertically distributed in two distinct layers, with different geodynamic origins. Fig. 6 overlays a schematic distribution of azimuthal anisotropy based on our model onto a North–South cross-section of the European Geophysical Traverse (EGT, Kissling et al., 2006). Seismic anisotropy is a macroscopic property, but its origin is related to microscopic properties of rocks. The two main sources of seismic anisotropy are shape-preferred orientation (SPO) of inclusions or cracks and lattice preferred orientation (LPO) of the rock aggregate minerals in response to large, regionally coherent strain. Because olivine, the most abundant mineral of the upper mantle, is anisotropic and orientates in its fast direction under applied shear (e.g., Barruol and Kern, 1996; Barberini et al., 2007), the LPO of olivine is usually advocated as the main source of anisotropy in the upper mantle. The anisotropy we observe north of the Alpine front at periods of 28 s and higher and beneath the central chain at periods of 32 s and higher is likely due to LPO of olivine related to the southward bending and subduction of the slab (Fig. 6). Amphiboles and biotite are present in the crust in a large proportion, and are strongly anisotropic (Nicolas and Christensen, 1987; Barruol and Mainprice, 1993). As a consequence, any preferred orientation is likely to result in strong seismic anisotropy (Sue et al., 1999). The orogen-parallel anisotropy we see beneath and north of the alpine front at periods up to 20 s, and the orogen-perpendicular anisotropy we observe beneath the Alpine arc in the range of 24–28 s, may thus result from LPO of amphiboles and/ or biotite. Interestingly, measurements performed on exposed samples from the Alpine lower crust indicate that LPO of amphibole is responsible for strong seismic anisotropy (Barberini et al., 2007). The orientation of filled cracks and other inclusions (SPO) is often considered to be the main source of anisotropy in the upper crust (e.g., Babuska and Cara, 1991; Crampin, 1994), and cannot be excluded as the origin of the anisotropy we observed up to periods of 16 s. In the
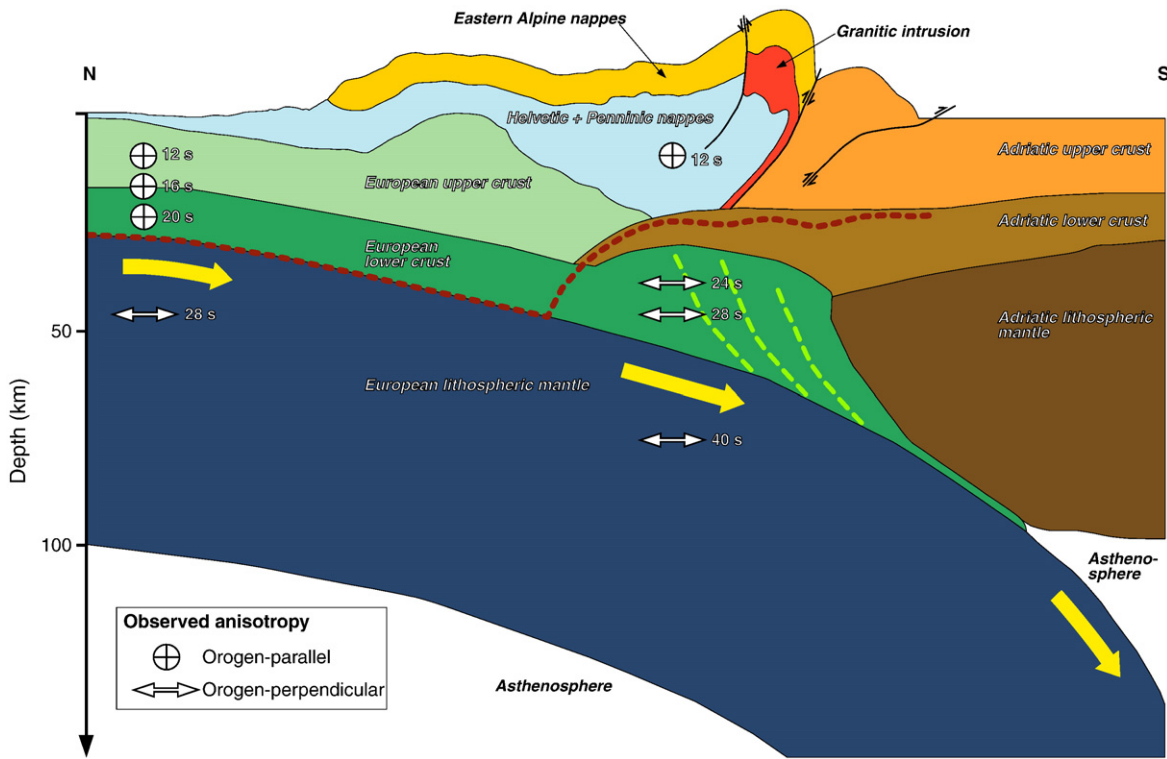
Fig. 6. Schematic interpretation of the European Geophysical Traverse (EGT) cross-section going from north to south across the Alps (modified from Kissling et al., 2006). Depth-dependent azimuthal anisotropy from our inversions is shown with arrows and crosshairs. Major crustal thrust faults are shown. The green dashed curves indicate delamination of the European lower crust from the underlying lithospheric mantle, which may be the source of the observed anisotropy beneath the central Alps in the range of 24–28 s. The brown dashed curve shows the lower limit of the seismicity observed in the past 40 years (e.g., Deichmann, 1992; Deichmann et al., 2000).
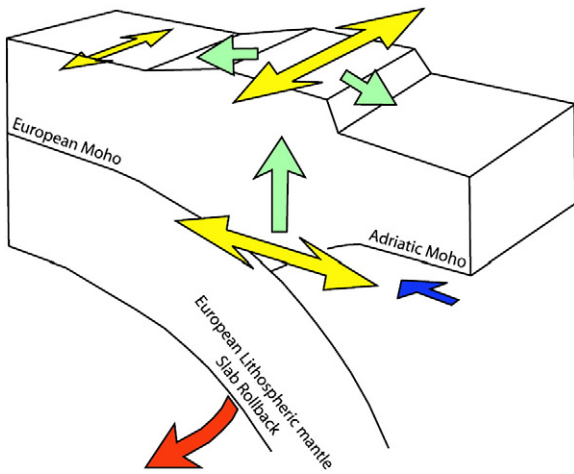
Fig. 7. Our inversion results, schematically shown with yellow arrows, are compatible with the tectonic model of Kissling, 2008. After delamination of the European lithospheric mantle, slab rollback (red arrow) and inward flow of Adriatic mantle generate orogen perpendicular anisotropy (lower yellow arrow) and positive buoyancy (green arrow) of the Alps. This leads to near-vertical emplacement of crustal slices (green dashed curves in Fig. 5), gravitational collapse of the orogen, and orogen parallel fast directions of anisotropy (upper yellow arrow).

upper crust, our Rayleigh-wave model cannot discriminate between SPO and LPO end-member hypotheses. Also shown in Fig. 6 is the approximate lower boundary of the observed seismicity beneath the Alps and its northern foreland during the past 40 years (Deichmann and Rybach, 1989; Deichmann, 1992; Deichmann et al., 2000; Schmid and Kissling, 2000). This limit gets suddenly shallower beneath the central chain, which may indicate a change in the rheology of the European and Adriatic lower crusts in this region, from brittle to ductile. Interestingly, this is correlated with the change in the direction of fast propagation in the European lower crust, from orogen-parallel in the northern foreland (16–20 s periods) to orogen-perpendicular beneath the central chain (24–28 s periods).

The regional and vertical distributions of the anisotropy we observe suggest that different fabrics are present in the central Alpine lithosphere, with different geodynamic origins. A possible origin for the orogen-parallel anisotropy beneath the central Alps in the range of 12–16 s is the LPO of crustal minerals (e.g., amphibole and biotite) in response to compression. The orogen-perpendicular anisotropy at 28 s and higher periods beneath the northern foreland and at 32 s and higher periods beneath the central chain may be due to LPO of olivine as a consequence of the southward bending and flow of the European lithospheric mantle.

A remarkable feature of the lower European crust north of the Alps is a high horizontal seismic reflectivity (Meissner et al., 1990; Prodehl et al., 1992; Mayer et al., 1997), which is attributed to alternating isotropic and anisotropic lamellae in the lower crust. This reflectivity is also seen in the northern Alpine foreland, but it disappears beneath the Alpine front (Holliger and Kissling, 1992; Pfiffner et al., 1997), i.e. the Alpine orogeny has overprinted the lower crust's reflectivity. Because it would be difficult to explain why the Alpine orogeny would have both induced seismic anisotropy and maintained the seismic reflectivity in the northern Alpine foreland, we argue that the anisotropy in this region has a pre-Alpine origin. A good candidate is the Hercynian orogeny (280–380 Ma), which is the major large scale episode of deformation that precedes the Alpine orogeny. Alternatively, it may be related to the Rhine Graben rifting episode, whose direction of extension is East–West, and which is associated with a strong seismic reflectivity (Mayer et al., 1997). Our model is however geographically too limited to provide a clear conclusion, and a continental scale anisotropic model of the European crust is needed to answer this question.

Kissling (2008) proposed a geodynamic model of the Alps that satisfies constraints based on geologic mapping, earthquake focal mechanisms (Jimenez-Munt et al., 2005), a strong positive Bouguer anomaly, a surplus of uplift compared to convergence (2 cm/year and 1.5 cm/year respectively), lithospheric balancing, and regional seismic observations (Lippitsch et al., 2003). In this model, Alpine subduction is locked, owing to relatively low slab pull and the geometry of the lower crustal indentor in the central and western Alps. The negative buoyancy of the European lithospheric mantle is driving detachment at the Moho (Fig. 7). The detachment is likely dynamically aided by the buttressing effect of the Ivrea crustal indentor. Detachment is progressing toward the northwest. Without the negative buoyancy of the lithosphere to counteract the positive buoyancy of the crust below the Alps, the European lower crust responds by uplifting in slices (represented by green dashed curves in Fig. 6). This crustal slicing and wedging mechanism is compatible with the orogen parallel anisotropy we see at periods in the range of 24–28 s (note that it also implies a vertical component, which we cannot map with Rayleigh wave). We argue that Adriatic mantle is drawn into the void left from the retreating European lithospheric mantle and drives the flow-parallel, orogen-perpendicular LPO of lower crust minerals, and the subsequent fast directions we see at periods in the range of 24–28 s (approximately 30 to 60 km depth).

Numerical modelling has been used to test models of indentor tectonics in the Alps by comparing computed geometry, crustal thickening, and uplift with that measured from topographic and seismological surveys. These models required non-linear strain-dependent rheology to reproduce measured uplift in the Alps and geometry of the orogen. The added buoyancy and concentrated zones of deformation generated during the crustal slicing we are proposing might allow a constant, temperature-dependent viscosity to be used for each unit as an alternative rheology during similar studies in the future.

We have combined ambient noise and anisotropic tomographic methods to map depth-dependent anisotropy in the lithosphere of the central Alps, and found that Rayleigh-wave azimuthal anisotropy in the central Alps is distributed in two dominant layers, suggesting different geodynamic origins. Deeper fabrics associated with the subducted the slab and underlying mantle, and sampled by larger periods (40–60 s) may also be present. However, lateral variations in this depth range are not resolvable by our current models. Merging noise interferometry and inversion for anisotropy is a promising technique for utilizing the increasing large number of dense regional deployments of broadband seismometers. Maps of both 'frozen' and 'active' crustal anisotropy should be capable of resolving many open questions about both current and previous tectonic events.

Acknowledgements

Appendix A. Supplementary data

Supplementary data associated with this article can be found, in the online version, at doi:10.1016/j.epsl.2010.06.008.

References

Babuska, V., Cara, M., 1991. Seismic anisotropy in the Earth. Kluwer Acad., Norwell, Mass. 217 pp.

Barberini, V., Burlini, L., Zappone, A., 2007. Elastic properties, fabric and seismic anisotropy of amphibolites and their contribution to the lower crust reflectivity. Tectonophysics 445, 227–244.

Barruol, G., Kern, H., 1996. Seismic anisotropy and shear-wave splitting in lower-crustal and upper-mantle rocks from the Ivrea Zone — experimental and calculated data. Phys. Earth Planet. Inter. 95, 175–194.

Barruol, G., Mainprice, D., 1993. 3-D seismic velocities calculated from lattice-preferred orientation and reflectivity of a lower crustal section: example of the Val Sesia section (Ivrea zone, northern Italy). Geophys. J. Int. 115, 1169–1188.

Boschi, L., Fry, B., Ekström, G., Giardini, D., 2009. The European upper mantle as seen by surface waves. Surv. Geophys 30 (4–5), 463–501. doi:10.1007/s10712-009-9066-2.

Christensen, N.I., 1984. The magnitude, symmetry and origin of upper mantle anisotropy based on fabric analyses of ultramafic tectonics. Geophys. J. R. Astron. Soc. 76, 89–112.

Coward, M., Dietrich, D., 1989. Alpine tectonics, an overview, in Alpine Tectonics. Geol. Soc. Lond. Spec. Publ. 45, 1–20.

Crampin, S., 1994. The fracture criticality of crustal rocks. Geophys. J. Int. 118, 428–438.

Darbyshire, F., Lebedev, S., 2009. Rayleigh wave phase velocity heterogeneity and multilayered azimuthal anisotropy of the Superior Craton, Ontario. Geophys. J. Int. 176, 215–234.

Davies, J.H., von Blanckenburg, F., 1995. Slab breakoff — a model of lithosphere detachment: its test in the magmatism and deformation of collisional orogens. Earth Planet. Sci. Lett. 129, 85–102.

Debayle, E., Kennett, B.L.N., Priestley, K., 2005. Global anisotropy and the thickness of continents. Nature 433, 509–512.

Deichmann, N., 1992. Structural and rheological implications of lower-crustal earthquakes below northern Switzerland. Phys. Earth Planet. Inter. 69, 270–280.

Deichmann, N., Rybach, L., 1989. Earthquakes and temperatures in the lower crust beneath the northern Alpine foreland of Switzerland. The lower crust: properties and processes. : In: Remeu, R.F., et al. (Ed.), Geophys. Monograph Ser., 51. American Geophysical Union, Washington D.C., pp. 197–213.

Deichmann, N., Baer, M., Braunmiller, J., Ballarin-Dolfin, B., Bay, F., Delouis, B., Fäh, D., Giardini, D., Kastrup, U., Kind, F., Kradolfer, U., Künzle, W., Röthlisberger, S., Schler, T., Salichon, J., Sellami, S., Spülher, E., Wiemer, S., 2000. Earthquakes in Switzerland and surrounding regions during 1999. Eclogae Geol. Helv. 93, 395–406.

Deschamps, F., Lebedev, S., Meier, T., Trampert, J., 2008a. Azimuthal anisotropy of Rayleigh-wave phase velocities in the East-central United States. Geophys. J. Int. 173, 827–843.

Deschamps, F., Lebedev, S., Meier, T., Trampert, J., 2008b. Stratified seismic anisotropy reveals past and present deformation beneath the East-central United States. Earth Planet. Sci. Lett. 274, 489–498.

Eberhart-Phillips, D., Reyners, M., 2009. Three-dimensional distribution of seismic anisotropy in the Hikurangi subduction zone beneath the central North Island, New Zealand. Journal of Geophysical Research 114 (B06301), 21. doi:10.1029/2008JB005947.

Fouch, M.J., Rondenay, S., 2006. Seismic anisotropy beneath stable continental interiors. Phys. Earth Planet. Inter. 158, 292–320.

Fry, B., Boschi, L., Ekström, G., Giardini, D., 2008. Europe-Mediterranean tomography: high correlation between new seismic data and independent geophysical observables. Geophys. Res. Lett. 35, L04301. doi:10.1029/2007GL031519.

Holliger, K., Kissling, E., 1992. Gravity interpretation of a unified 2-D acoustic image of the central Alpine collision zone. Geophys. J. Int. 111, 213–225.

Jimenez-Munt, I., Garcia-Castellanos, D., Negredo, A.M., Platt, J.P., 2005. Gravitational and tectonic forces controlling postcollisional deformation and the present-day stress field of the Alps: constraints from numerical modelling. Tectonics 24, TC5009. doi:10.1029/2004TC001754.

Kissling, E., 2008. Deep structure and tectonics of the Valais — and the rest of the Alps. Swiss Bull. Appl. Geol. 13 (2), 3–10.

Kissling, E., Schmid, S.M., Lippitsch, R., Ansorge, J., Fügenschuh, B., 2006. Lithosphere structure and tectonic evolution of the Alpine arc: new evidence from high-resolution teleseismic tomography. Geological Society, London, Memoirs 32, 129–145. doi:10.1144/GSL.MEM.2006.032.01.08.

Lebedev, S., Van Der Hilst, R.D., 2008. Global upper-mantle tomography with the automated multimode inversion of surface and S-waveforms. Geophys. J. Int. 173, 505–518.

Lippitsch, R., Kissling, E., Ansorge, J., 2003. Upper mantle structure beneath the Alpine orogen from high-resolution teleseismic tomography. J. Geophys. Res. 108, B2376. doi:10.1029/2002JB002016.

Lobkis, O., Weaver, R., 2001. On the emergence of the Green's function in the correlations of a diffuse field. J. Acoust. Soc. Am. 110, 3011–3017.

Marone, F., Romanowicz, B., 2007. The depth distribution of azimuthal anisotropy in the continental upper mantle. Nature 447, 198–203.

Mayer, G., Mai, P.M., Plenefisch, T., Echtler, H., Lüschen, E., Wehrle, V., Müller, B., Bonjer, K.-P., Prodehl, C., Fuchs, K., 1997. The deep crust of the Southern Rhine Graben: reflectivity and seismicity as images of dynamic processes. Tectonophycs 275, 15–40.

Meier, T., Dietrich, K., Stöckhert, B., Harjes, H.-P., 2004. One-dimensional models of shear wave velocity for the eastern Mediterranean obtained from the inversion of Rayleigh wave phase velocitites and tectonic implications. Geophys. J. Int. 156, 45–58.

Meissner, R., Wever, T., Sadowiak, P., 1990. Reflectivity patterns in the Variscan mountain belts and adjacent areas: an attempt for a pattern recognition and correlation to tectonic units. Tectonophysics 173, 361–378.

Montagner, J.-P., Tanimoto, T., 1991. Global upper mantle tomography of seismic velocities and anisotropies. J. Geophys. Res. 96, 20337–20351.

Nicolas, A., Christensen, N.I., 1987. Formation of anisotropy in upper mantle peridotites — a review. Composition, structure and dynamics of the Lithosphere-Asthenosphere system: In: Fuchs, K., Froidevaux, C. (Eds.), American Geophysical Union, pp. 111–123.

Paige, C.C., Saunders, M.A., 1982. LSQR: an algorithm for sparse linear equations and sparse least squares. ACM Trans. Math. Softw. 8, 43–71.

Pedersen, Bruneton, M., Maupin, V., the SVEKALAPKO Seismic Tomography Working group, 2006. Lithospheric and sublithospheric anisotropy beneath the Baltic shield from surface-wave array analysis. Earth Planet. Sci. Lett. 244, 590–605.

Peter, D., Boschi, L., Deschamps, F., Fry, B., Ekström, G., Giardini, D., 2008. Surface-wave tomography: finite-frequency shear-velocity inversions for the European–Mediterranean region. Geophys. Res. Lett. 35, L16315. doi:10.1029/2008GL034769.

Pfiffner, O.A., Lehner, P., Hitzmann, P., Mueller, S., Steck, A., 1997. Deep structure of the Alps: results from NRP 20. Birkhäuser, Basel, Switzerland. 380 pp.

Piromallo, C., Morelli, A., 2003. P wave tomography of the mantle under the Alpine–Mediterranean area. J. Geophys. Res. 108, B2065. doi:10.1029/2002JB001757.

Prodehl, C., Mueller, S., Glahn, A., Gutscher, M., Haak, V., 1992. Lithospheric cross-sections of the European Cenozoic rift system. Tectonophysics 208, 113–138.

Sabra, K.G., Gerstoft, P., Roux, P., Kuperman, W.A., Fehler, M.C., 2005. Extracting timedomain Green's function estimates from ambient seismic noise. Geophys. Res. Lett. 32. doi:10.1029/2004GL021862.

Sanchez-Sesma, F.J., Perez-Ruiz, J., Campillo, M., Luzon, F., 2006. Elastodynamic 2-D Green function retrieval from cross-correlation: canonical inclusion problem. Geophys. Res. Lett. 33, L13305. doi:10.1029/2006GL026454.

Savage, M.K., 1999. Seismic anisotropy and mantle deformation: what we have learned from shear-wave splitting. Rev. Geophys. 37, 65–106.

Schmid, S.M., Kissling, E., 2000. The arc of the western Alps in the light of geophysical data on deep structure. Tectonics 19, 62–85.

Shapiro, N.M., Campillo, M., Stehly, L., Ritzwoller, M., 2005. High resolution surface wave tomography from ambient seismic noise. Science 307, 1615–1618.

Silver, P.G., 1996. Seismic anisotropy beneath the continents: probing the depths of geology. Annu. Rev. Earth Planet. Sci. 24, 385–432.

Simons, F.J., van der Hilst, R.D., Montagner, J.-P., Zielhuis, A., 2002. Multimode Rayleigh-wave inversion for heterogeneity and azimuthal anisotropy of the Australian upper mantle. Geophys. J. Int. 151, 738–754.

Smith, M.L., Dahlen, F.A., 1973. Azimuthal dependence of Love and Rayleigh wave propagationvin a slightly anisotropic medium. J. Geophys. Res. 78, 3321–3333.

Snieder, R., 2004. Extracting the Green's function from the correlation of coda waves: a derivation based on stationary phase. Phys. Rev. Lett. E69, 046610.

Stehly, L., Campillo, M., Shapiro, N., 2006. A study of the seismic noise from its long range correlation properties. J. Geophys. Res. 111, B10306. doi:10.1029/2005JB004237.

Stehly, L., Fry, B., Campillo, M., Shapiro, N., Guilbert, J., Boschi, L., Giardini, D., 2009. Tomography of the Alpine region from observations of seismic ambient noise. Geophys. J. Int. 178, 338–350.

Sue, C., Thouvenot, F., Frechet, J., Tricart, P., 1999. Widespread extension in the core of the western Alps revealed by earthquake analysis. J. Geophys. Res. 104, 25611–25622.

Trampert, J., Lévêque, J.-J., 1990. Simultaneous iterative reconstruction technique: physical interpretation based on the generalized least square solution. J. Geophys. Res. 95, 12553–12559.

Trampert, J., Woodhouse, J.H., 2003. Global anisotropic phase velocity maps for fundamental modes surface waves between 40 and 150 seconds. Geophys. J. Int. 154, 154–165.

Waldhauser, F., Kissling, E., Ansorge, J., Mueller, S., 1998. Three-dimensional interface modelling with two-dimensional seismic data: the Alpine crust mantle boundary. Geophys. J. Int. 135, 264–278.

Wang, Z., Dahlen, F.A., 1995. Validity of surface-wave ray theory on a laterally heterogeneous Earth. Geophys. J. Int. 123, 757–773.

Wortel, M.J.R., Spakman, W., 1993. Subduction and slab detachment in the Mediterranean-Carpathian region. Science 290, 1910–1917.

Yang, Y., Forsyth, D.W., 2006. Rayleigh-wave phase velocities, small-scale convection, and azimuthal anisotropy beneath southern California. J. Geophys. Res. 111, B7306. doi:10.1029/2005JB004180.

Yao, H., van der Hilst, R., 2009. Analysis of ambient noise energy distribution and phase velocity bias in ambient noise tomography, with application to SE Tibet. Geophys. J. Int. doi:10.1111/j.1365-246X.2009.04329.x.

Yao, H., van der Hilst, R., de Hoop, M.V., 2006. Surface-wave array tomography in SE Tibet from ambient seismic noise and two-station analysis — I. Phase velocity maps. Geophys. J. Int. doi:10.1111/j.1365-246X.2006.03028.x.

Zhang, X., Paulssen, H., Lebedev, S., Meier, T., 2007. Surface wave tomography of the Gulf of California. Geophys. Res. Lett. 34, L15305. doi:10.1029/2007GL030631.